UC Berkeley

UC Berkeley Previously Published Works

Title

Picometer sensitivity metrology for EUV absorber phase

Permalink

https://escholarship.org/uc/item/2p42q3sr

Journal

Journal of Micro/Nanopatterning Materials and Metrology, 20(3)

ISSN

1932-5150

Authors

Sherwin, Stuart

Cordova, Isvar

Miyakawa, Ryan

et al.

Publication Date

2021-07-01

DOI

10.1117/1.jmm.20.3.031011

Peer reviewed

eScholarship.org Powered by the California Digital Library
University of California

Picometer sensitivity metrology for EUV absorber phase

Stuart Sherwin[a,*] **Isvar Cordova**[b] **Ryan Miyakawa**[b] **Markus Benk**[b] **Laura Waller**[a] **Andrew Neureuther**[a] **and Patrick Naulleau**[b]

[a]University of California Berkeley, Department of Electrical Engineering and Computer Science, Berkeley, California, United States

[b]Center for X-Ray Optics, Lawrence Berkeley National Laboratory, Berkeley, California, United States

Abstract. With growing interest in EUV attenuated phase-shift masks due to their superior image quality for applications such as dense contact and pillar arrays, it is becoming critical to model, measure, and monitor the intensity and relative phase of multilayer and absorber reflections. We present a solution based on physical modeling of reflectometry data, which can achieve single picometer phase precision and sensitivity to changes in average film thickness below one atomic monolayer. We measure absorber and multilayer reflectivity to determine thin-film parameters with a multidimensional optimization and then acquire a new measurement of either multilayer or absorber to determine perturbations in surface contamination thickness. While it is difficult to assess the accuracy of the first step, the simplicity of the second step allows us to characterize our sensitivity to changes in contamination thickness. We apply this analysis using an initial set of measurements and repeated measurements after a period of storage. For the multilayer, the total contamination growth was 1068 pm, which occurred almost exclusively during storage (1085 pm) and decreased very slightly during repeated measurements (−17 pm). For the absorber, the behavior was quite different, with a total growth of 126 pm, which occurred much less during storage (28 pm) and primarily during repeated measurements (98 pm). Ultimately, the change in relative phase (absorber minus multilayer) was −0.86 deg for the multilayer and −1.12 deg for the absorber. We estimate the precision of the surface contamination measurement to be $3\sigma < 6$ pm for measuring thickness and $3\sigma < 0.2$ deg for measuring phase.

1 Introduction

In recent years, interest in EUV attenuated phase-shift masks (aPSMs) has increased, particularly for small-pitch dense patterns.[1] A traditional absorber cannot create a high contrast image without substantial bias due to the relative imbalance of the zero-order and scattered waves. An aPSM on the other hand uses destructive interference between the pattern (absorber) and the background (multilayer), thus reducing the power of the zero-order and transferring that power into the scattered waves. Therefore, an aPSM offers both higher contrast and throughput than a traditional absorber for these critical patterns.[1] And yet the introduction of EUV aPSMs requires addressing the challenges of precisely measuring and controlling the phase. Particularly, we are concerned with the relative phase between the absorber and multilayer reflections at a defined reference plane, which we in this work take to be the topmost surface of the photomask, including both the absorber and any contamination that might be present.

We present a reflectometry-based metrology solution that can measure the relative phase between multilayer and absorber with single picometer precision. The method requires measurements of the absorber and multilayer reflectivity under varying illumination conditions. These

*Address all correspondence to Stuart Sherwin, stuartsherwin@berkeley.edu

measurements are then used in a multidimensional nonlinear least-squares regression to determine a possible physical model for the multilayer and absorber; we can then compute the Fresnel reflectance from the physical model to extract the relative phase of multilayer and absorber. Subsequent measurements of the absorber and multilayer can then be used to determine changes in the surface contamination thickness from a brute-force single-dimensional nonlinear least-squares regression.

While the claim of extracting phase from measurements of only amplitude may at first seem dubious, the Kramer's-Kronig relations imply that there is a unique relationship between the phase and amplitude of an analytic function (such as, the reflection coefficient).[2] Therefore, any analytic function that matches the measured amplitude over a sufficiently large wavelength range must match the phase of the true reflection coefficient. By construction, our computed Fresnel coefficient will always be analytic, because it is composed of analytic functions of the tabulated atomic scattering factors,[3] which are themselves analytic. Furthermore, our Fresnel coefficient cannot be simply any analytic function; it is greatly restricted in what values it can take on by prior knowledge of the mask. Prior knowledge comes in several forms: the known wavelength-dependence of each material's refractive index, the nominal thickness for each layer, and a measurement of the top surface roughness conducted by atomic force microscopy (AFM). This allows us to restrict the range of variables, which given strict enough bounds should mitigate remaining ambiguities so that any solution that matches the measured reflectivity for both multilayer and absorber to sufficient accuracy within the variable bounds should also provide an accurate prediction of the relative phase.

At the same time, there is certainly still room for further studies into the absolute accuracy to assess the exact requirements on the range of illumination conditions and prior knowledge. Additional prior knowledge could also be obtained from supplemental measurements such as grazing incidence reflectometry to measure the refractive index. So while we expect that the initial multidimensional optimization should be able to accurately measure the phase given enough data and enough prior information, nonetheless to quell any remaining fears about the uniqueness of the solution to the multidimensional optimization, we restrict our major claims to the precision of the secondary single-dimensional nonlinear least-squares regression used to determine changes in contamination thickness on the top surfaces of the absorber and multilayer. In this way, we hope to demonstrate that at the very least our approach is highly repeatable and sensitive to small changes while leaving the door open to future studies into absolute accuracy.

We validated our technique on a test mask that has a standard 40 bilayer Mo-Si multilayer mirror and a 60-nm TaN absorber. We performed an initial reflectivity measurement for the multilayer and 2 months later for the absorber. After an additional 3 months, we repeated both multilayer and absorber measurements back-to-back. We observed a substantial change in the multilayer signal during storage, but during the repeated measurements, the signal was relatively stable. In contrast, the absorber changed systematically during both storage and measurement.

We hypothesized that the most likely explanation for contamination would be a thin carbon film growing on top of the multilayer and absorber, based on previous studies of carbon contamination on EUV multilayers and Ta-based absorbers depending on storage conditions and EUV exposure.[4–6] Therefore from this point forward, we hold all other parameters constant and adjust only the carbon layer thickness on either the multilayer or absorber when assessing the repeatability of the technique; this assumption allows us to use a simple brute-force search that guarantees convergence to a unique optimal solution (given a fixed initial model and a set of reflectivity measurements). This allows us to quantify changes in the carbon film thickness and the relative phase. During storage, we estimate the change in carbon contamination thickness to be 1068 pm for the multilayer (over 5 months) and 28 pm for the absorber (over 3 months). During the reflectivity measurement, the contamination rates were approximately

-1.7 pm/measurement (11 measurements) for the multilayer and 12.3 pm/measurement (9 measurements) for the absorber. We estimate an overall change in the relative phase of -0.86 ± 0.1 deg $[3\sigma]$ for the multilayer and -1.12 ± 0.16 deg $[3\sigma]$ for the absorber.

Section 2 defines the mask geometry and experimental conditions. Section 3 defines the mathematical model and optimization approach. In Sec. 3.1, we describe the Fresnel coefficient

model and the mean-squared error (MSE) objective function used in our optimization. In Sec. 3.2, we discuss our choice of optimization algorithm for the initial multidimensional optimization. We wrap up discussion of computational methods in Sec. 3.3, where we describe the brute-force search used for the carbon contamination measurements. Section 4 presents the results of both optimization steps. In Sec. 4.1, we present the initial model, which demonstrates the ability of our technique to find at least some solution matching the measured reflectivity. Then, in Sec. 4.2, we show clear trends revealed by the brute-force search for carbon contamination on the absorber and multilayer. In Sec. 5, we analyze the phase recovered from the modeled Fresnel coefficient. In Sec. 5.1, we define the effective propagation distance of the reflection coefficient for both multilayer and absorber and discuss some of its implications on imaging. In Sec. 5.2, we discuss how this single absorber has not one but a range of phase values for different illumination conditions. In Sec. 5.3, we describe the interference effects in multilayer and absorber reflections, particularly how transmission alone is insufficient to predict the relative phase or to model the impact of contamination. Finally, in Sec. 5.4, we quantify the precision of our method, considering random and systematic error.

2 Experimental Methods

We characterize an EUV photomask using measurements of reflectivity from pure multilayer and absorber regions on the mask, taken at the Advanced Light Source Calibration, Optics Testing and Spectroscopy Beamline 6.3.2.[7] In each reflectivity measurement, we illuminate a flat spot on the photomask with a defined wavelength and angle of incidence and measure the reflected intensity; we sequentially repeat this process over a range of wavelengths and angles to produce a scan of reflectivity.

Figure 1 shows a cross-sectional view of measuring multilayer and absorber reflectivity. The reflectometer measures the amplitude-squared of the reflection coefficient of each region; our goal is to extract the relative phase between these two reflections. To define the phase, we must specify a reference plane, which we define as the topmost surface of the photomask. Although this reference plane may not necessarily coincide with the plane of best focus, it is a very natural choice because it is the lowest possible reference plane that is completely above the surface. If we assume an absorber of thickness t and index of refraction $\tilde{n} = 1 + \delta - i\beta$, then the relative phase would be $2tk_z\delta$ (the factor of 2 arising due to reflection). However, as discussed in Sec. 5.3, it is not sufficient to only consider light transmitted through the absorber, because there is also a substantial effect due to interference with light reflected by the absorber, which is captured in the rigorous Fresnel reflection coefficient calculation. One counterintuitive aspect of this approach to keep in mind is that the reference plane now depends on the thickness of contamination on the absorber; if the focal plane was not adjusted to compensate, then in the far-field image you would observe changes in both phase (scattering) and focus (imaging).

The multilayer nominally consists of a 2.5-nm Ru cap as well as 40× Mo–Si bilayers; the "bilayers" actually contain four layers rather than two in our model, as an additional MoSi interdiffusion layer is added at both the Mo–Si and Si–Mo interfaces.[8] The absorber has an additional 58-nm TaN absorber topped with a 2-nm TaON antireflection coating (ARC) layer; note that the ARC is to reject out-of-band DUV light and not to suppress the reflection of EUV. The measured

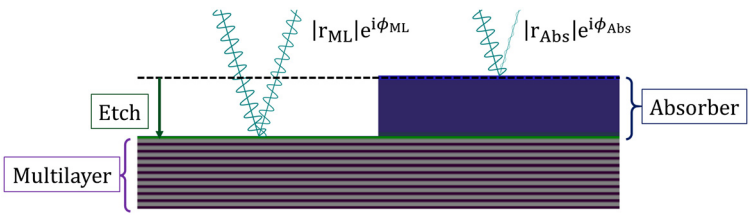

Fig. 1 Photomask schematic depiction of reflections from absorber and multilayer. Absorber layers from top to bottom are: TaON–TaN–Ru–(Si–MoSi–Mo–MoSi)x40. Multilayer uses the same film-stack, with an additional etch depth parameter to replace etched layers with vacuum. Additional C layers are added on top of the absorber and multilayer, representing contamination.

"multilayer" is actually an absorber that has been etched, so we model this with an additional etch depth parameter, which can either represent residual TaN thickness (if positive) or reduced Ru thickness (if negative); the nominal value is −0.2 nm, meaning that nominally the Ru would be 0.2 nm thinner after etch than it is under the absorber. We further place a layer of pure carbon on top of the absorber and multilayer to represent contamination.

The refractive index of each layer is based on the atomic composition of the layer and the atomic scattering factors of the constituent elements.[3,9] We use the atomic scattering factors, f_0, f_1, in the Center for X-Ray Optics database to capture the wavelength-dependent changes in absorption and refraction for each element.[3] For soft x-ray and EUV wavelengths, the refractive index can be approximated as $n = 1 - \delta + i\beta = 1 - \frac{n_a r_a \lambda^2}{2\pi}(f_0 + if_1)$, where n_a is the atomic density, r_a is the Bohr radius, and λ is the wavelength; in the case of a multiatomic material, one can then sum up the impact of each material on δ and β.[10] For each material, m, we define a nominal concentration $n_{a,m}$, which, together with the tabulated scattering factors $f_{0,m}$, $f_{1,m}$, determines a nominal refractive index: $n_m = 1 - \delta_m + i\beta_m = 1 - \frac{n_{a,m} r_a \lambda^2}{2\pi}(f_{0,m} + if_{1,m})$. If a layer is composed of a set of materials, where material m has an atomic density of $w_m n_{a,m}$, we compute the refractive index with a weighted sum: $n = 1 - \delta + i\beta = 1 - (\sum_m w_m[\delta_m - i\beta_m])$. Our model contains a total of $N = 101$ wavelengths, $M = 7$ materials, and $K = 10$ layers, meaning that we must predict a total of 1010 values for a complex refractive index. The above model suggests that we may greatly reduce the dimension of the problem by controlling each layer's wavelength-dependent complex refractive index, $\mathbf{N} \in \mathbb{C}^{N\times K}$, via the much smaller matrix, of each layer's concentration of each element, $\mathbf{W} \in \mathbb{R}^{M\times K}$, and a matrix containing the nominal $\delta - i\beta$ for each material, $\mathbf{A} \in \mathbb{C}^{N\times M}$. $(\mathbf{N})_{n,k}$ is the complex refractive index in layer k at wavelength n; $(\mathbf{W})_{m,k}$ is the concentration of element m in layer k; and $(\mathbf{A})_{n,m}$ is $\delta - i\beta$ for element m at nominal atomic density for wavelength n. Finally, we compute the wavelength-dependent refractive index matrix for all layers as $\mathbf{N} = \mathbf{1} - \mathbf{AW}$. Because most layers consist of only one or two materials, only 14 of 70 concentration matrix elements are nonzero, allowing us to control a 1010-element complex valued matrix $\mathbf{N}$ via only 14 positive real numbers in $\mathbf{W}$. We report the fitted concentration values in 7.3, and in Table 1, we report the resulting refractive index of each layer at $\lambda = 13.5$ nm.

Table 1 Physical model for the film-stack. "Multilayer" layers (Ru, Si, MoSi, Mo, MoSi) are common to absorber and etch. On top of these are either the three "absorber" layers (C, TaON, TaN) or "etch" layers (Vac, C, TaN). If TaN (Etch) is positive, then some absorber remains unetched; on the other hand if it is negative (as it is here) then some of the Ru has been etched. Roughness is RMS surface roughness. Index of refraction at $\lambda = 13.5$ nm is $n = 1 - \delta + i\beta$.

	Thickness	Roughness	Delta	Beta
C (absorber)	1.683	0.327	0.046	0.008
TaON (absorber)	1.857	0.373	0.028	0.020
TaN (absorber)	58.110	0.346	0.046	0.033
Vac (etch)	58.105	0.000	0.000	0.000
C (etch)	3.854	0.159	0.046	0.008
TaN (etch)	-0.311	0.000	0.046	0.033
Ru (multilayer)	2.151	0.141	0.120	0.018
Si (multilayer)	3.625	0.136	0.001	0.002
$MoSi_2$ (multilayer)	0.568	0.140	0.025	0.004
Mo (multilayer)	1.858	0.141	0.074	0.006
$MoSi_2$ (multilayer)	0.919	0.138	0.029	0.005

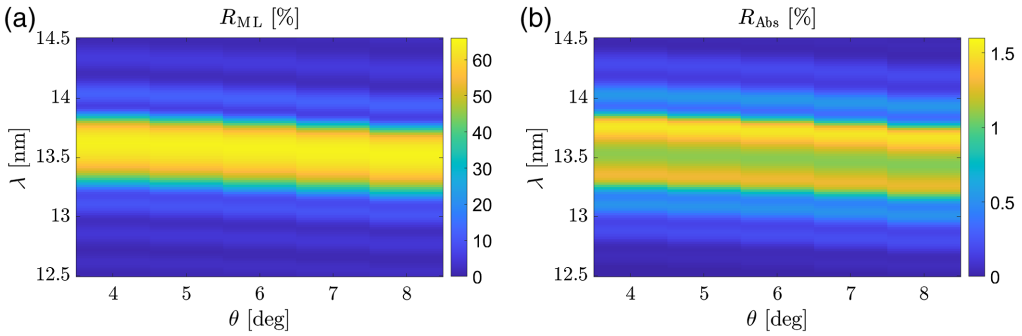

Fig. 2 Reflectometry raw data scan of wavelength (y) and angle (x) for (a) multilayer and (b) absorber. Note that the absorber reflectivity differs strikingly from the multilayer, with a drop in reflectivity near the multilayer's peak. This is due to destructive interference between a dominant component reflected by the multilayer and attenuated by the absorber transmission squared, and a much weaker modulation component reflected from the absorber only.

Nominal roughness values were obtained by AFM measurement of the top surface, which found 134 pm of RMS roughness on the multilayer and 382 pm on the absorber. The 134 pm of roughness on the multilayer was also used to apply a constant 1.95% reflectance loss to the multilayer (impacting both multilayer and absorber reflections), based on previous empirical measurements of power losses due to replicated surface roughness in EUV masks.[11] The final thickness, roughness, and refractive index of each layer are listed in Table 1. The full table of fitted parameters is also listed in 7.3.

We measure the reflectivity for both multilayer and absorber over a range of wavelengths (12.5 to 14.5 nm) and angles (4 deg to 8 deg), shown in Fig. 2. We carried out our measurements multiple times to characterize changes over time as well as precision. Ultimately, we acquired an initial multilayer measurement, followed 2 months later by an initial absorber measurement, followed 3 months later by an additional 11 multilayer and 9 absorber measurements at the same mask locations collected back-to-back (all multilayer followed by all absorber measurements). Note that a dotted line is used to connect absorber measurements 8 and 9, when the light source was temporarily down.

We observe the reflectivity in both absorber and multilayer regions changing over time, shown in Fig. 3; here, R_0 denotes the initial reflectivity measurement for all wavelengths and angles, and R_i denotes the i'th subsequent measurement. We plot the data both in terms of the RMS change over all wavelengths and angles [Fig. 3(a)], as well as the average change again over all wavelengths and angles [Fig. 3(b)]. The RMS change ($= \sqrt{\langle R_i^2 - R_0^2 \rangle}$) is a metric of the distance of R_i from R_0, adding up the magnitude of change across the entire signal and can only be positive; the average change ($= \langle R_i - R_0 \rangle$) sums up all changes to reflectivity regardless of where they occur in the signal, and it can be either positive (increased total power) or negative (decreased total power). There is a 4.6% RMS (−0.89% average) change in the multilayer signal as a result of storage between the initial measurement and the subsequent measurements (5 months) but then relatively little change over the remaining measurements. The trend for the absorber on the other hand is quite different: there is a relatively smaller 3.4% RMS (+2.7% average) change after the first measurement (3 months), followed by a clear increasing trend for both metrics. This suggests that contamination of the multilayer occurred almost exclusively during storage, whereas contamination of the absorber occurred both during storage and exposure. Also note that whereas the multilayer reflectivity decreases on average due to contamination, the absorber reflectivity actually increases, which can only be understood by considering the interference between the reflected and transmitted components in the absorber, further described in Sec. 5.3.

We hypothesize that the changes in both the multilayer and absorber are likely due to carbon contamination on the top surface, which has been observed growing in both storage[4,6] and during exposure,[4] as well as being cleaned during exposure in a scanner environment.[6] The differing contamination behaviors observed for multilayer and absorber are intriguing. Regarding the seemingly faster contamination rate of the multilayer during storage, we refrain from speculating

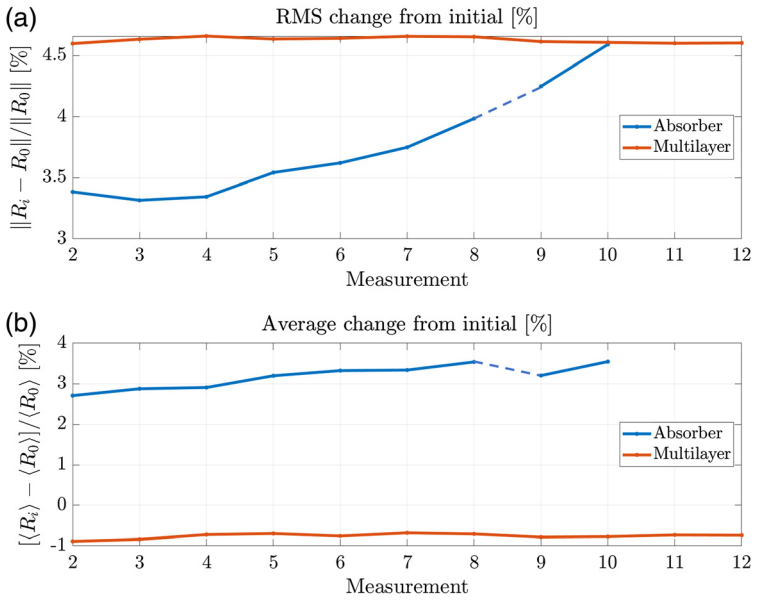

Fig. 3 Changing reflectivity over time for multilayer and absorber. R_0 denotes the initial reflectivity for all wavelengths and angles, and R_i denotes the i'th subsequent measurement. The multilayer experiences a change of 4.6% RMS (−0.89% average) as a result of storage (5 months), but then relatively little change over the remaining measurements. On the other hand, for the absorber there is a relatively smaller change of 3.4% RMS (+2.7% average) after the first measurement (3 months), followed by an increasing trend for both metrics. A dotted line is used to connect absorber measurements 8 and 9, when the light source was temporarily down.

due to insufficient data. On the other hand, there is a clear physical explanation for why we would observe the steady contamination during reflectivity measurement only in the absorber due to its much higher EUV absorption, which should create a steady stream of escaping secondary electrons that can "crack" hydrocarbon molecules in the chamber and allow freed carbon to bind to the surface.

3 Computational Methods

3.1 *Problem Statement*

We parametrize each layer of our mask by a thickness and a concentration of each elemental species and parametrize each interface by its RMS surface roughness. Given all these physical parameters, we compute the Fresnel reflection coefficient[12–14] and compare its amplitude to a measurement of reflectivity versus wavelength (λ) and angle (θ). We then perform an iterative optimization to find a set of physical parameters that minimizes the MSE. We write the error $\mathcal{E}$ as

$$\mathcal{E}(x_1, x_2, \ldots, x_m) = \frac{1}{n}\sum_{i=1}^{n}\left[|r(x_1, x_2, \ldots, x_m; \lambda_i, \theta_i)| - \sqrt{R_{\text{meas}}(\lambda_i, \theta_i)}\right]^2,$$

where $x_1, x_2, \ldots, x_m$ are the unknown variables, r computes the Fresnel reflection coefficient, R_{meas} is the measured reflectivity, and $\{\lambda_i, \theta_i\}_{i=1}^n$ are the measured pairs of wavelengths and angles. We express our nonlinear least squares optimization problem as

$$\min_{x_1,\ldots,x_m} \mathcal{E}(x_1, \ldots, x_m).$$

3.2 *Initial Multidimensional Optimization*

We choose a relatively simple yet seemingly robust method for our optimization, namely cyclic coordinate descent,[15] solving each one-dimensional (1D) subproblem with golden-section search.[16,17] In this method, we cycle through the unknown parameters (cyclic), optimizing the function with respect to only one parameter at a time (coordinate descent). We initialize with $\{x_j^0\}_{j=1}^m$ and obtain $\{x_j^k\}_{j=1}^m$ after k complete cycles. In each cycle, we loop through all coordinates and update one at a time. The subproblem for unknown x_j on iteration k is

$$\min_{x_j} \mathcal{E}(x_1^k, \ldots, x_{j-1}^k, x_j, x_{j+1}^{k-1}, \ldots, x_m^{k-1}) = \min_{x_j} f_{j,k}(x_j).$$

We solve each 1D subproblem with a golden-section search, which is a derivative-free optimization technique closely related to binary search.[16,18] The well-known zero-finding algorithm binary search shrinks the distance between two points by a factor of 2 each iteration and converges to a zero, and the golden-section search shrinks the distance by a factor of the golden ratio $\phi = \frac{1+\sqrt{5}}{2}$ each iteration and converges to a local minimum between the initial bounds. We denote the golden-section search algorithm as

$$x^* = \mathrm{GSS}[f(\cdot), L, U, N],$$

where $f(\cdot)$ is the function to be minimized, L is the initial lower bound, U is the initial upper bound, and N is the number of iterations. The algorithm is outlined in detail in 7.1.

In each iteration, we apply this suboptimization to $f_{j,k}$, using bounds centered around the current iterate x_j^{k-1}, with a radius $\Delta_{j,k} = \Delta_j \gamma^{k-1}$ such that $L = x_j^{k-1} - \Delta_{j,k}$ and $U = x_j^{k-1} + \Delta_{j,k}$. Here, Δ_j is the initial search radius, which is chosen to be a fraction β ($0 < \beta < 1$) of the distance between the upper and lower variable bounds, UB_j and LB_j, respectively: $\Delta_j = \beta(\mathrm{UB}_j - \mathrm{LB}_j)$. On each iteration, the search radius shrinks by a factor of γ ($0 < \gamma < 1$), making the search on each iteration more refined than the previous. We write this suboptimization as

$$x_j^* = \mathrm{GSS}[f_{j,k}(\cdot), x_j^{k-1} - \Delta_{j,k}, x_j^{k-1} + \Delta_{j,k}, N].$$

After completing the golden-section search, we update x_j with a convex combination of the previous and new value using some α ($0 < \alpha < 1$):

$$x_j^k = \alpha x_j^* + (1 - \alpha) x_j^{k-1}.$$

In practice, we use an α value slightly below 1 (e.g., 0.9), which is equivalent to slightly reducing the step size for each update. Reducing the α value slows down convergence but generally helps improve the stability. An advantage of this approach is that golden-section search does not require us to perform any cumbersome gradient or Jacobian computations for the Fresnel reflection coefficient (unlike other approaches such as gradient descent or Gauss–Newton).[19]

3.3 *Contamination Measurement*

After performing this multidimensional optimization based on the initial multilayer and absorber measurements only, we freeze all parameters except the thickness of carbon contamination. Then for each measurement, we perform a brute-force search, evaluating a range of thicknesses from 0 to 8 nm and choosing the thickness with the lowest MSE. For measuring the contamination on the absorber, we use the first multilayer measurement and change only the measurement of the absorber and vice versa for contamination on the multilayer. The simple brute-force optimization algorithm used in this final step should help allay fears about the physical accuracy of the initial optimization, because any remaining errors in the physical parameters are held constant for all measurements. All claims about sensitivity and precision to thickness and phase are based solely only on this secondary brute-force optimization (which is guaranteed to find the global optimum), rather than the initial multidimensional optimization (which is not). Furthermore,

regardless of the physical correctness of the global optimum of this function, as long as there is a sufficient gap in MSE from the next lowest local minimum, then the global optimum will be chosen robustly and the precision will simply be due to the curvature of the minimum and the noise in the measurement, exactly like a linear regression. Still, we acknowledge that unless almost all physical parameters are known in advance, this reflectometry phase measurement may not be absolutely accurate but should remain highly repeatable and sensitive to small changes. Future work is still needed to study the absolute accuracy of this method, and it is possible that accuracy can only be guaranteed with additional measurements, for example, AFM to measure the surface roughness (which is included in these results) or grazing incidence reflectometry to measure the refractive index (which is not).

4 Results

4.1 *Initial Optimization*

We perform our initial fit on the first reflectivity scan only (each consisting of 505 measurements) for multilayer and absorber, fitting 31 physical parameters using in total 1010 reflectivity measurements. We specify initial values as well as upper and lower bounds for each variable (listed in 7.3), which restricts the domain of our search to a 31-dimensional box. We then loop through variables updating one at a time iteratively to increase the fidelity of the model to the measured reflectivity as described in Sec. 3.2 and 7.2. The predicted amplitude of the initial fit is shown in Fig. 4 alongside the experimental measurement. Note that both experiment and fit are plotted as a function of k_z ($= 2\pi \cos\theta/\lambda$), whereas the actual experimental data are collected as a function of both λ and θ. This simplification is possible because over this measurement range the reflectance has very little dependence on the transverse wave vector due to the planar symmetry and the relatively small range of measured angles. We perform this compression only for ease of visualization, which is to say that the actual Fresnel coefficient calculation takes into account both the wavelength and angle. This approximation does lead to a faint amount of apparent "noise" in Fig. 4, which is in fact not noise but rather the manifestation of slight reflectance variation orthogonal to k_z. While there is certainly no mathematical guarantee about the uniqueness of our solution, Fig. 4 shows that our optimization procedure can at least find some physical solution consistent with the data. More likely than not some physical parameters may be "compensating" for others and possibly introducing some systematic errors in the prediction. However, this issue (if present) could be resolved given a sufficiently accurate initial guess and sufficiently tight bounds on each variable, which may require that additional supplementary measurements be performed. The final physical model for thickness, roughness, and refractive index is presented in Table 1, but again we stress that this is merely one possible physical model rather than the only possibility consistent with the data.

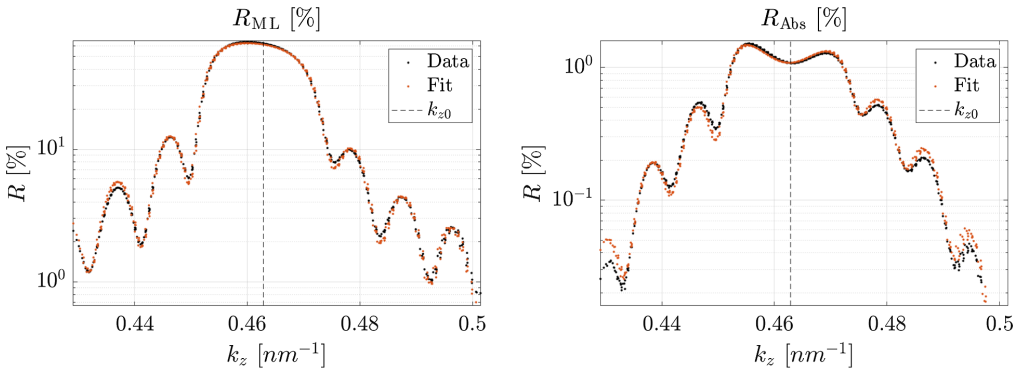

Fig. 4 Modeled reflectivity versus k_z. Comparison of raw (black) and fitted (red) reflectivity based on initial 31 parameter fit, demonstrating the ability to find a solution consistent with the data.

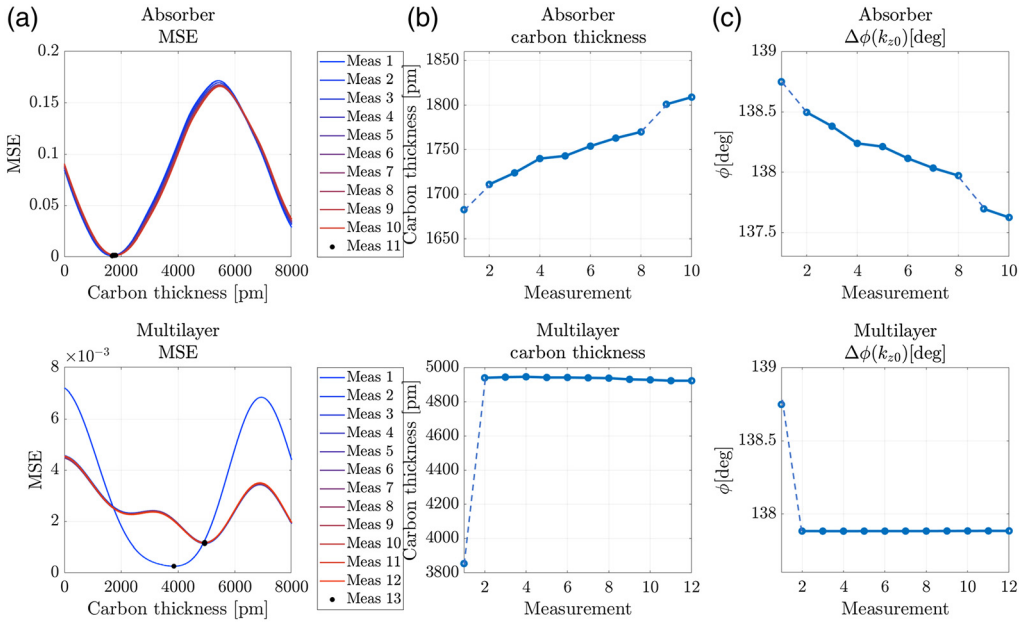

Fig. 5 Carbon growth on multilayer (top) and absorber (bottom): single parameter fit to model contamination. (a) MSE versus carbon thickness; black dots show optimal value for each measurement. (b) Recovered carbon thickness: increases sharply for multilayer during storage but not measurement; increases systematically during both storage and measurement for absorber. A dotted line is used to connect data points before and after storage, and in the absorber between measurements 8 and 9 when the light source was temporarily down. (c) Relative phase between absorber and multilayer; total change of -0.86 deg for multilayer and -1.12 deg for absorber.

4.2 *Contamination Measurement*

Following this initial optimization, we freeze the model and perform a brute-force search for the carbon contamination thickness corresponding to each multilayer and absorber measurement. This is shown in Fig. 5 for multilayer (a) and absorber (b). The leftmost plot shows the MSE versus carbon thickness for each measurement, and the black dots show the optimal values. For the multilayer, there is a clear separation between the first and later measurements, whereas all the absorber measurements are closely clustered. The middle plot shows the carbon contamination thickness for each measurement, which clearly shows the sharp jump in contamination on the multilayer as opposed to the steady increase on the absorber. The rightmost plot shows how the contamination impacts the relative phase value (absorber phase minus multilayer phase). The multilayer contamination causes the phase to jump down by -0.86 deg and then remain approximately constant, whereas the absorber contamination causes the phase to gradually decrease by -1.12 deg. Note that both are changing in the same direction, meaning that the combining the two effects would imply a -1.98 deg change in the relative phase.

Two somewhat counterintuitive observations arrive from these results: first, a smaller change in the absorber contamination thickness (126 versus 1068 pm) causes a larger change in the phase (-1.12 deg versus -0.86 deg); and second, the growth of the same material on absorber and multilayer causes the same sign of change in the relative phase (absorber phase minus multilayer phase). Both these apparent mysteries are caused by interference effects, discussed in Sec. 5.3. If we accounted only for transmission, then the phase shift from a change in thickness would be $(\pm)2tk_z\delta$, corresponding to $+0.31$ deg and -2.59 deg for the absorber and multilayer, respectively. As expected, the signs are opposite, and the magnitude of the change in phase is proportional to the change in thickness. But the interference impacts both the multilayer and absorber reflections, leading to a smaller value with the same sign for the multilayer (-0.86 deg versus -2.59 deg) and a larger value with opposite sign for the absorber (-1.12 deg versus $+0.31$ deg). These substantial deviations from the simplified transmission

model can be attributed to interference effects in the reflection, which are explored further in Sec. 5.3.

As to the question of how we could possibly be sensitive to thickness changes smaller than an atomic monolayer, the answer is that we are measuring an average thickness across the area of the beam. While the contamination must consist of an integer number of atoms, due to nonuniformity, it need not consist of an integer number of atomic monolayers. In this way, we can detect changes averaging only a fraction of a monolayer across the beam spot.

5 Analysis

5.1 *Effective Propagation Distance*

From our initial model, we can extract the phase as a function of k_z, shown in Fig. 6. In addition to the relative phase shift between multilayer and absorber at the nominal operating condition $k_{z0} = 2\pi \cos 6 \text{ deg } /(13.5 \text{ nm})$, we can also use our model to obtain useful information about mask three-dimensional (3D) effects from the partial derivative $\partial\phi/\partial k_z$. This derivative represents an effective propagation distance for each reflection coefficient. The effective propagation distance for the multilayer is 240 nm, including both reflection by the multilayer and transmission twice through vacuum of equal height to the absorber. The propagation distance for the absorber on the other hand is 279 nm, an increase of 39 nm (17%). Pattern translation as a function of illumination angle is proportional to this propagation distance ($\Delta x = \frac{\partial\phi}{\partial k_z} \tan\theta$), meaning that for this mask light reflected from the absorber will translate 17% further than light reflected from the multilayer, which should impact mask 3D (M3D) effects. Bear in mind, however, that these numbers, as they are derived from the initial optimization, which is not guaranteed to find a uniquely optimal solution, must still be taken with a grain of salt and should be further confirmed with other measurements. It may be the case that the actual numbers differ from those presented. However, the same qualitative effects would be present albeit with possibly a different magnitude.

5.2 *Phase Variation Across the Source*

In addition to impacting M3D effects, the 39-nm difference in effective propagation distance between multilayer and absorber will cause the pattern phase to depend on the illumination condition, that is to say the same absorber will have different phases from different source points. Variation in k_z across the source could arise from variation in either angle or wavelength. For this mask, a 2% change in wavelength would cause a phase shift of $\Delta\phi_\lambda = (\partial\phi/\partial k_z)k_0(2\%) = 21.0$ deg. A change in angle from one edge of the pupil to the other (Y,

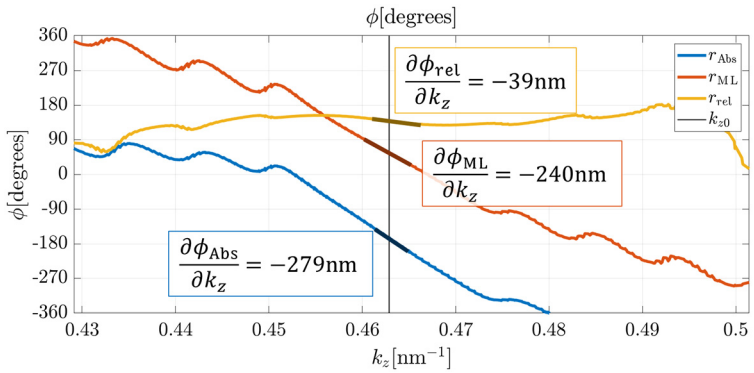

Fig. 6 Recovered phase based on fitted Fresnel reflection coefficient from initial 31 parameter fit for absorber (blue), multilayer (red), and relative (yellow). The partial derivative $\partial\phi/\partial k_z$ represents an effective propagation distance. The absorber has a significantly larger effective propagation distance than the multilayer (279 versus 240 nm), which will impact the M3D effects.

Table 2 Phase change across source for the 0.33 and 0.55 NA systems, based on recovered $\partial\phi_{\text{rel}}/\partial k_z = 39$ nm. For both systems, a 2% λ variation leads to a 21.0 deg variation in the phase. The 0.33 NA system also has substantial variation in the Y direction (18.3 deg) but much less in X (3.6 deg). In contrast, in the 0.55 NA system the variation is reduced in Y (13.5 deg) but greatly increased in X (10.1 deg)

NA	$\Delta\phi_\lambda$[2%] (deg)	$\Delta\phi_{\theta_y}$ (deg)	$\Delta\phi_{\theta_x}$ (deg)	m_y	m_x	θ_0 (deg)	$\theta_y^{\max}$ (deg)	$\theta_x^{\max}$ (deg)
0.33	21.0	18.3	3.6	4	4	6.0	10.7	7.7
0.55	21.0	13.5	10.1	8	4	5.355	9.3	9.6

shadowing orientation) would cause a phase shift of $\Delta\phi_{\theta_y} = (\partial\phi/\partial k_z)k_0[\cos\,\theta_{\min} - \cos\,\theta_{\max}] = 18.3$ deg and 13.5 deg for the 0.33 and 0.55 NA systems, respectively; the effect is somewhat mitigated in the higher NA system due to the increased magnification and decreased chief-ray angle. On the other hand, we observe the opposite trend in the X direction due to increased mask-side NA, where the variation increases from 3.6 deg to 10.1 deg. These effects are summarized in Table 2.

The fact that images from different illumination angles (and wavelengths) can span such a wide range of phase shifts will surely have consequences for imaging and therefore should be considered in designing future EUV aPSMs. Quantifying the severity of these effects and exploring options for mitigation are open-ended problems that surely merit further study; here, we propose just a few possible strategies for mitigation. In the case of low k_1 (where there is the most interest in EUV aPSMs to begin with), the required illumination will introduce substantial M3D effects in source points far from normal incidence (positive u_y); it may be possible to equalize the contrast for source points with positive and negative u_y by designing the absorber phase primarily for positive-u_y source points at the expense of the negative where M3D effects are less severe to begin with. Another strategy, which could perhaps best accommodate arbitrary sources, would be to design an absorber whose phase varies more slowly versus k_z, which would reduce the magnitude of this effect overall; in principle, this should be possible, particularly if one were willing to use a more complicated absorber architecture. Finally, if the resolution permits, one could simply restrict the source to reduce k_z variation without redesigning the absorber.

5.3 *Interference Effects*

To interpret the multilayer and absorber reflection coefficients, a simplified "transmission-only" analysis will not suffice. For both the multilayer and absorber, we must consider the interference between different reflections, which is rigorously accounted for in the Fresnel coefficient calculation via the transfer matrix method[12] in which each layer (j) is described by a 2×2 transfer matrix M_j, and the overall reflection or transmission through a stack of layers is computed from the product of all transfer matrices: $M = \Pi_j M_j$. Due to the associativity of matrix multiplication, we may group together any set of layers without modifying the final result, so we define three matrices M_{ML}, M_{Abs}, and M_{Etch}, which each contains the product of transfer matrices in the respective group of layers.

The multilayer consists of $N = 40$ repetitions of a four-layer unit cell (Si–MoSi–Mo–MoSi): $M_{\text{ML}} = (\Pi_{j=1}^{4} M_{\text{ML},j})^N$. The absorber consists of four layers (C–TaON–TaN–Ru): $M_{\text{Abs}} = \Pi_{j=1}^{4} M_{\text{Abs},j}$. And the etch consists of three layers (Vac–C–Ru): $M_{\text{Etch}} = \Pi_{j=1}^{3} M_{\text{Etch},j}$. The final transfer matrix in the absorber region of the mask is $M_{\text{Abs}}M_{\text{ML}}$, and in the multilayer region it is $M_{\text{Etch}}M_{\text{ML}}$. The reflection from the transfer matrix is then given by $r = M_{2,1}/M_{1,1}$, and the transmission is given by $t = 1/M_{1,1}$.

A simplified "transmission-only" analysis would be equivalent to considering only $t_{\text{Abs0}} = 1/M_{\text{Abs1,1}}$ and $t_{\text{Etch0}} = 1/M_{\text{Etch1,1}}$, then taking the ratio $t_{\text{Abs0}}^2/t_{\text{Etch0}}^2$. However, this approach does not capture the impact of interference between reflections from different layers, which can be

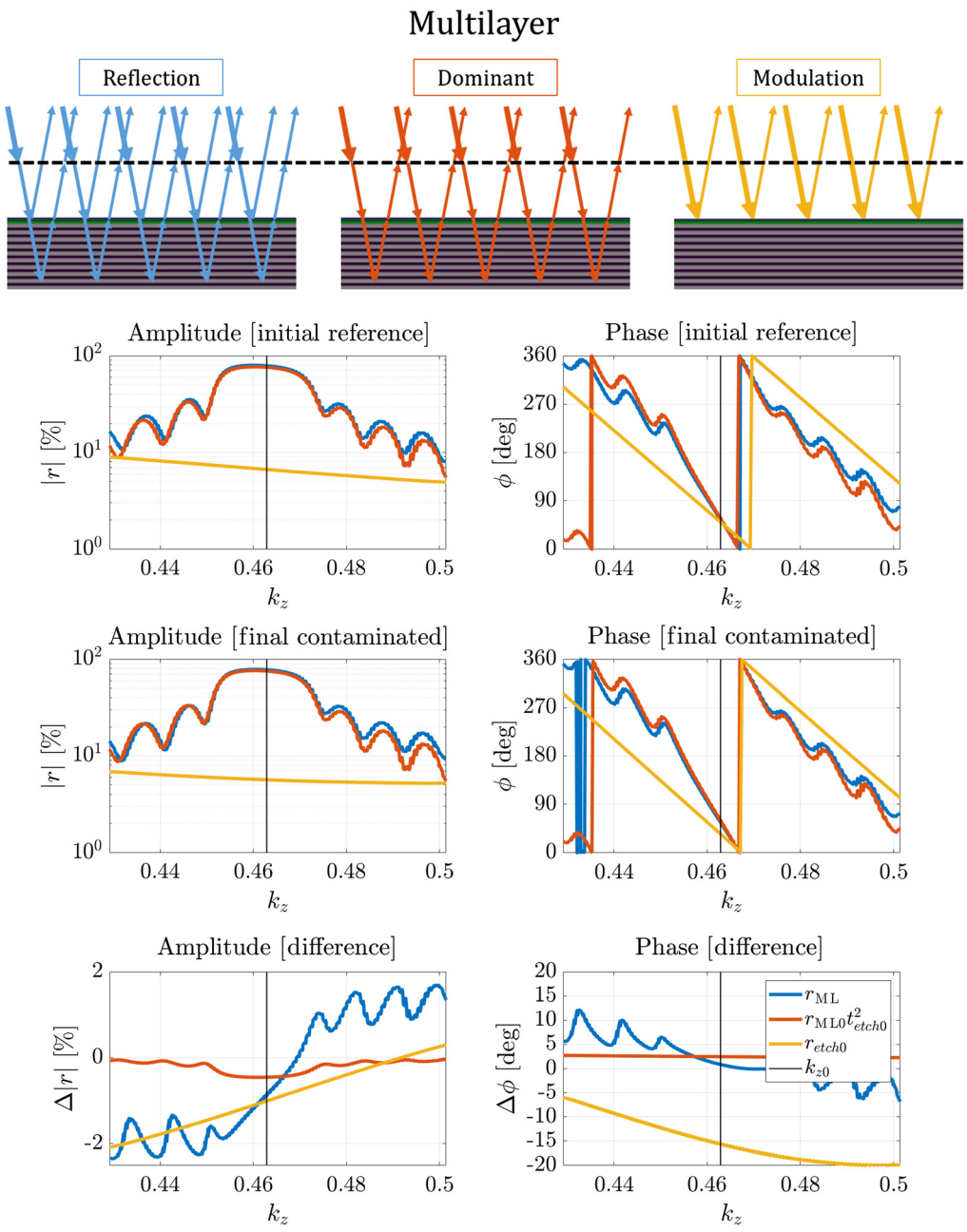

Fig. 7 Schematic illustration of decomposing multilayer reflection into dominant and modulation components. Initial measurement: the amplitude of the dominant component is approximately the amplitude of the multilayer reflection coefficient, whereas the amplitude of the modulation component is approximately linear with k_z. Final measurement: after the growth of ~1 nm of carbon, the amplitude of both components decreases uniformly. Difference: both the dominant and modulation components are attenuated, but the overall reflection has increased amplitude for high k_z and decreased amplitude for low k_z. Phase changes in opposite directions for the dominant and modulation components, reducing the final change in phase. The final phase change contains a slope due to the different effective propagation distances in the two components.

substantial, such as the destructive interference visible in the absorber reflectivity. A slightly more advanced approach that can begin to explain these interference effects is to consider the final reflection as the sum of two components: a dominant component that transmits twice and is reflected by the multilayer and a much weaker modulation component that is reflected before interacting with the multilayer. We write these components for the absorber as $t^2_{\mathrm{Abs0}} r_{\mathrm{ML0}}$ and

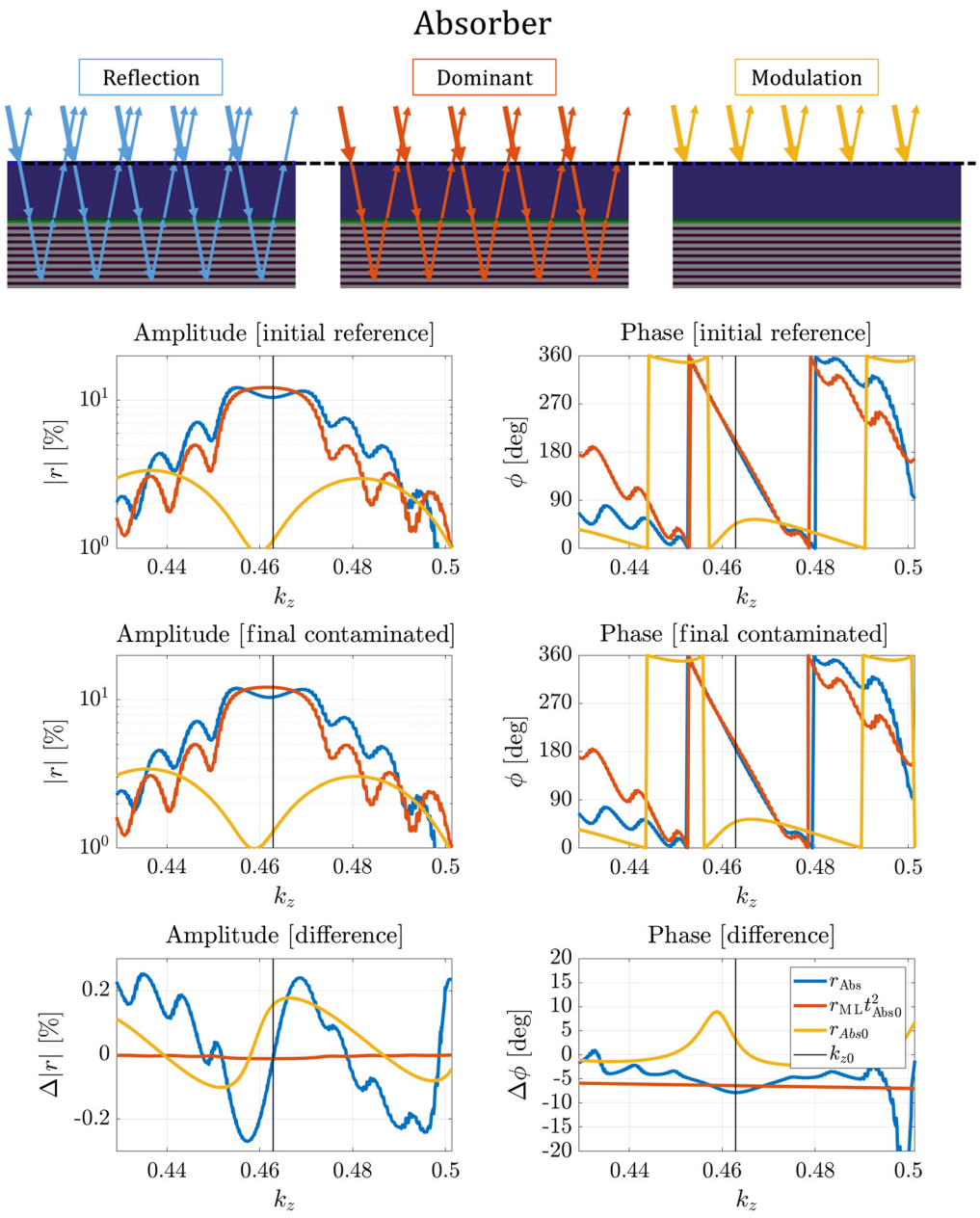

Fig. 8 Schematic illustration of decomposing absorber reflection into dominant and modulation components. Initial measurement: the amplitude of the dominant component closely follows the amplitude of the multilayer reflection coefficient, whereas the amplitude of the modulation component has additional features, such as the local minimum at k_{z0} (due to interference between the four layers composing the absorber). Final measurement: after the growth of ~100 pm of carbon, there is a slight change in the relative intensities of the two highest peaks. Difference: observe the changes due to contamination from final minus initial model. The left peak decreases and the right peak increases by a similar amount. There are substantial changes in both modulation component amplitude and the phase of both components.

r_{Abs0}, and for the etch as $t^2_{\mathrm{Etch0}} r_{\mathrm{ML0}}$ and r_{Etch0}, where r_{ML0}, r_{Abs0}, and r_{Etch0} are $M_{2,1}/M_{1,1}$ for the corresponding transmission matrix. This allows us to introduce the approximate reflection equations $r_{\mathrm{abs}} \approx t^2_{\mathrm{abs0}} r_{\mathrm{ML0}} + r_{\mathrm{abs0}}$ and $r_{\mathrm{ML}} \approx t^2_{\mathrm{etch0}} r_{\mathrm{ML0}} + r_{\mathrm{etch0}}$.

This interference process is shown in Figs. 7 and 8, which show the total reflection (blue) with its dominant (red) and modulation (yellow) components. Note that all three components are calculated from the product of multiple transfer matrices, so each component itself contains

interference between multiple layers; furthermore, the approximate decomposition into dominant and modulation components is purely for illustration, and the approximation is not used in computing the final reflection.

In the case of the multilayer region, shown in Fig. 7, the final reflection is almost entirely due to the dominant component, because the C and Ru have well over 90% transmittance but less than 10% reflectance. This leads to the relative imbalance of the dominant multilayer reflection ($t_{\text{etch0}}^2 r_{\text{ML0}}$) and the much smaller modulation (r_{etch0}). The greater slope $\partial\phi/\partial k_z$ of the dominant component implies that it has a larger effective propagation distance, which is expected due to the effective reflection plane of the multilayer.

As a result of contamination, both the dominant and modulation components are attenuated, but the overall reflection has increased amplitude for high k_z and decreased amplitude for low k_z. This overall amplitude change is due to the interference between the two components, specifically because the phase between the two components is decreased for high k_z and increased for low k_z. The dominant component phase increases by roughly a constant, but the modulation component phase decreases by a much larger amount in roughly a parabolic trend. This causes the overall change in phase at k_{z0} to be much smaller than the change in phase from the dominant component, hence why the simplified transmission-only analysis greatly overpredicts the change in phase. Also note that the phase change of the final reflection has an overall negative slope with k_z, implying that the overall propagation distance is increased, i.e., the surface contamination appears to push the reflection plane deeper into the multilayer.

In the case of the absorber, as shown in Fig. 8, the interference plays an even greater role in forming the final reflection. Whereas the dominant absorber component is roughly just an attenuated version of the multilayer, the final reflection amplitude oscillates around this value, with a local minimum approximately where the multilayer attains its maximum. This local minimum is easily observed in the raw data and is caused by destructive interference between the dominant ($t_{\text{abs0}}^2 r_{\text{ML0}}$) and modulation ($r_{\text{abs0}}$) components. The components interfere destructively because at k_{z0} (black vertical line) the phases of the dominant and modulation components are almost exactly 0 deg and 180 deg, respectively. Also note that there is substantial k_z variation in the absorber modulation component itself; this would not be the case if it were simply a reflection from the very top interface; however, k_z variation arises because the modulation component itself includes interference from the four layers comprising the absorber (C–TaON–TaN–Ru), captured in the transfer matrix calculation.

Contamination on the absorber results in a negligible change to the amplitude of the dominant component but a noticeable phase shift due to the additional optical path length of transmission through carbon. On the other hand, the total amplitude clearly shows the left peak decreasing and the right peak increasing (which is easily observable in the measured reflectivity data). A similar trend is also seen in the changes to the modulation component amplitude, but the final reflection has additional oscillations due to interference. The changes in the phase of the final reflection oscillate by several degrees around the changes to the dominant component, again demonstrating the importance of a rigorous Fresnel analysis rather than a simplified transmission-only analysis to assess phase effects.

5.4 *Precision*

In computing the precision, we exclude the initial measurements for both multilayer and absorber to remove the impact of storage. In addition, we compute the 3σ precision in two ways: using the raw data and using the residuals of a linear fit. Before taking the linear residuals, the 3σ for contamination thickness is 8.0 and 30.8 pm for the multilayer and absorber, respectively, but after removing the linear trend we obtain a better estimate of only the random component of the variation, 3.5 and 5.8 pm. So the sensitivity to thickness on both multilayer and absorber surfaces appears to be roughly similar and <6 pm. The corresponding precision for phase after accounting for the linear trend is 0.16 deg for the absorber and <0.1 deg for the multilayer (Fig. 9). However, the multilayer result being so low is likely not a general phenomenon, but rather seems to be specific to interference effects in the multilayer reflection, whereby increasing the contamination thickness shifts the phase of the dominant and modulation components of the multilayer reflection in opposite directions leading to a reduced overall phase shift. So the absorber

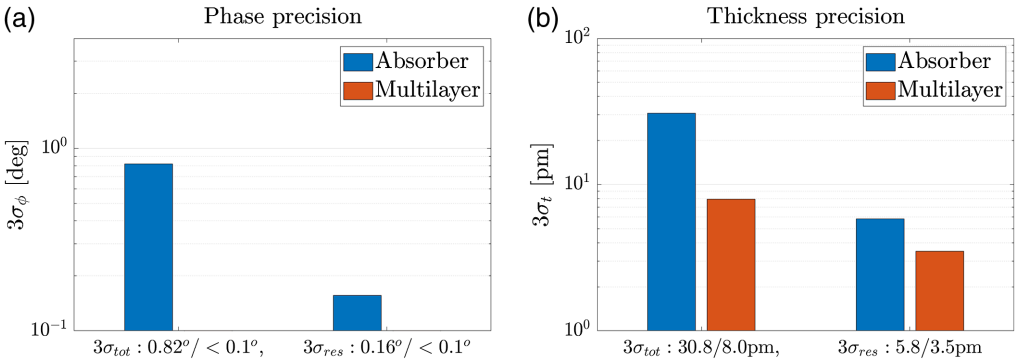

Fig. 9 Precision 3σ of total and linear residuals for (a) multilayer and absorber relative phase and (b) contamination thickness. First data point has been removed to remove the impact of storage and only consider precision of repeated measurements. Taking the linear residuals is a rough way to separate a systematic trend from noise. The multilayer trend has $3\sigma < 0.1$ deg whether or not we take the linear residuals. The absorber trend is highly systematic, so the precision is greatly reduced from the raw data ($3\sigma = 0.82$ deg) by taking the linear residuals (0.16 deg). Thickness precision considering the linear residuals is $3\sigma = 5.8$ and 3.5 pm for the multilayer and absorber, respectively.

precision of 0.16 deg should be seen as the more representative estimate for the phase precision of the technique.

6 Conclusion

We have presented a computational reflectometry technique to characterize the phase of an EUV photomask via measurements of reflectivity from multilayer and absorber regions. A 31 parameter physical model was capable of producing a highly accurate match to the experimental reflectivity data, although further studies are required to understand the absolute accuracy of the model because the optimization is not guaranteed to find a uniquely optimal solution. We used the physical model to extract the relative phase of the absorber and multilayer reflections, as well as the phase partial derivative with respect to k_z, which represents an effective propagation distance for each reflection coefficient. According to our model, the effective propagation into the absorber (279 nm) is 39 nm further than the multilayer (240 nm); among other things this will cause the phase to vary across the source. We then held our initial physical model fixed and used a brute-force search to measure carbon contamination on the multilayer and absorber; this simplified algorithm can guarantee convergence to a unique optimum for each measurement. We found that the multilayer was contaminated substantially more during storage than the absorber (1068 versus 28 pm), whereas during repeated EUV reflectometry measurements the contamination actually slightly decreased on the multilayer but continued growing on the absorber (-1.7 pm/measurement versus 12.3 pm/measurement). Although changes in absorber thickness amounted to only a fraction of an atomic monolayer, we were able to measure the average thickness of a nonuniform layer across the beam-spot to subatomic precision. Finally, we used repeated measurements to quantify the method's precision. The precision in measuring the contamination thickness determined by the linear residuals was $3\sigma = 3.5$ and 5.8 pm for the multilayer and absorber. The precision for measuring phase based on the contamination thickness was $3\sigma = 0.16$ deg for the absorber and >0.1 deg for the multilayer. Therefore, we have demonstrated single picometer precision for measuring both contamination thickness ($3\sigma < 6$ pm) and phase ($3\sigma < 0.2$ deg $= 7.5$ pm wavefront).

7 Appendix

An archived version of the code and data used to generate results and figures can be freely accessed and executed through Code Ocean: https://codeocean.com/capsule/8800481/tree

7.1 *Golden-Section Search Algorithm*

7.2 *Multidimensional Optimization Algorithm*

Inputs:

$f(\cdot)$ - Function to minimize

L - Initial lower bound

U - Initial upper bound

N - Number of iterations

$a = L$ # Lower bound

$b = U$ # Upper bound

$\phi = \frac{\sqrt{5}+1}{2}$ # Golden ratio

for $i = 1:N$ # Loop over N iterations

  $c = b - \frac{b-a}{\phi}$ # Left intermediate point

  $d = a + \frac{b-a}{\phi}$ # Right intermediate point

  if $f(c) < f(d)$ # c is more optimal than d

    $b = d$ # Reduce upper bound

  else # d is is more optimal than c

    $a = c$ # Increase lower bound

return $\text{argmin}\left[f(a), f(b), f\left(b - \frac{b-a}{\phi}\right), f\left(a + \frac{b-a}{\phi}\right)\right]$ # Return local optimum

---

Inputs:

$\{x_j^0\}_{j=1}^m$ - Initial parameter values

$\{\text{LB}_j\}_{j=1}^m$ - Lower bound for each parameter

$\{\text{UB}_j\}_{j=1}^m$ - Upper bound for each parameter

M - Number of overall (outer-loop) iterations

N - Number of iterations of GSS

β - Sets initial search radius

γ - Decay rate for search radius

α - Step size reduction for parameter update

$\{\Delta_j = \beta(\text{LB}_j - \text{UB}_j)\}_{j=1}^m$ # Initial search radius for each parameter

for $k = 1:M$ # Outer loop

  for $j = 1:m$ # Cycle through coordinates

    $\Delta_{j,k} = \Delta_j \gamma^{k-1}$ # New search radius

    $L = \max(x_j^{k-1} - \Delta_{j,k}, \text{LB}_j)$ # Lower bound

    $U = \min(x_j^{k-1} + \Delta_{j,k}, \text{UB}_j)$ # Upper bound

    $f_{j,k}(\cdot) = \mathcal{E}(x_1^k, \ldots, x_{j-1}^k, \cdot, x_{j+1}^{k-1}, \ldots, x_m^{k-1})$ # Function to minimize

    $x_j^* = \text{GSS}[f_{j,k}(\cdot), L, U, N]$ # Sub-problem

    $x_j^k = \alpha x_j^* + (1-\alpha) x_j^{k-1}$ # Update parameter value

return $\{x_j^M\}_{j=1}^m$ # Return final parameter vector

Hyperparameter values used were: $\alpha = 0.9$, $\beta = 0.02$, $\gamma = 2^{-1/25} \approx 0.97$. The computational complexity of this algorithm is $\mathcal{O}(mnMN)$, where m is the number of parameters, n is the number of measured data points, M is the number of overall iterations, and N is the number of iterations of golden-section search. The runtime has the same scaling except it is also multiplied by the time τ to compute the Fresnel coefficient for a single illumination condition.

Computations were carried out in Matlab on a Lenovo T470p running Windows X with an Intel i7 CPU running at 2.9 GHz. The unit computation time was $\tau = 23$ μs; scaling factors were

Table 3

	Minimum	Nominal	Fit	Maximum
Thickness (nm) C (absorber)	0.000	1.390	1.683	6.000
Thickness (nm) TaON (absorber)	1.000	2.000	1.857	3.000
Thickness (nm) TaN (absorber)	56.000	58.000	58.110	60.000
Thickness (nm) Ru (absorber)	1.500	2.500	2.151	3.500
Thickness (nm) Si (mirror)	3.427	3.627	3.625	3.827
Thickness (nm) $MoSi_2$ (mirror)	0.468	0.568	0.568	0.668
Thickness (nm) Mo (mirror)	1.658	1.858	1.858	2.058
Thickness (nm) $MoSi_2$ (mirror)	0.819	0.919	0.919	1.019
Thickness (nm) Vac (etch)	−0.500	−0.200	−0.311	0.100
Thickness (nm) C (etch)	0.000	4.410	3.854	6.000
Roughness (nm) C (absorber)	0.272	0.381	0.327	0.534
Roughness (nm) TaON (absorber)	0.272	0.381	0.373	0.534
Roughness (nm) TaN (absorber)	0.272	0.381	0.346	0.534
Roughness (nm) Ru (absorber)	0.096	0.134	0.141	0.188
Roughness (nm) Si (mirror)	0.096	0.134	0.136	0.188
Roughness (nm) $MoSi_2$ (mirror)	0.096	0.134	0.140	0.188
Roughness (nm) Mo (mirror)	0.096	0.134	0.141	0.188
Roughness (nm) $MoSi_2$ (mirror)	0.096	0.134	0.138	0.188
Roughness (nm) C (etch)	0.096	0.134	0.159	0.188
Concentration (%) TaON - Ta (absorber)	0.00	33.33	49.13	200.00
Concentration (%) TaON - N (absorber)	0.00	33.33	61.59	200.00
Concentration (%) TaON - O (absorber)	0.00	33.33	2.89	200.00
Concentration (%) TaN - Ta (absorber)	0.00	82.29	81.28	200.00
Concentration (%) TaN - N (absorber)	0.00	82.29	112.73	200.00
Concentration (%) Ru - Ru (absorber)	0.00	100.00	107.65	200.00
Concentration (%) Si - Si (mirror)	0.00	100.00	132.63	200.00
Concentration [%] $MoSi_2$ - Si (mirror)	0.00	66.67	89.52	200.00
Concentration (%) $MoSi_2$ - Mo (mirror)	0.00	33.33	31.68	200.00
Concentration (%) Mo - Mo (mirror)	0.00	100.00	97.45	200.00
Concentration (%) $MoSi_2$ - Si (mirror)	0.00	66.67	125.74	200.00
Concentration (%) $MoSi_2$ - Mo (mirror)	0.00	33.33	35.94	200.00

$n = 505$, $m = 31$, $M = 200$, $N = 20$, giving a total run time of approxi-mately $\tau mnMN \approx 24$ min.

7.3 *Table of Parameters*

Table 3 contains the minimum, maximum, nominal, and fitted values for all adjustable parameters in the multi-dimensional optimization. Fitted values correspond to the model presented in Table 1. Note that the fitted values should be regarded as merely one possible solution that fits the data while keeping in mind that other solutions may also be possible.

Notes on modeling: Layers listed from top to bottom. Roughness is RMS roughness of the interface above the listed surface. Concentration is as a percentage of a nominal concentration; n and k are calculated using a weighted sum of delta and beta from the CXRO database,[3] as described in Ref. 9. Vac (Etch) thickness represents the etch depth, relative to the top of the Ru capping layer. If it is 0, then the etch perfectly stops at the Ru; a negative value (as we have in the fit) implies the Ru layer been partially etched; whereas a positive value implies an incomplete etch. In this fit, the Ru capping layer is decreased by 0.31 nm from 2.15 to 1.84 nm after etch. Note once again that this solution represents merely one possible physical solution consistent with the data, and others may also be possible.

Columns from left to right are parameter name, lower bound for optimization, initial value (nominal), fitted value, and upper bound for optimization.

Acknowledgments

This research was sponsored by Intel Corporation. This work was performed in part at Lawrence Berkeley National Laboratory, which is operated under the auspices of the Director, Office of Science, of the U.S. Department of Energy under Contract No. DE-AC02-05CH11231. This paper was based on the conference presentation of the same name, presented at SPIE Photomask Technology + EUV Lithography, 2020. Proceedings Volume 11517, Extreme Ultraviolet Lithography 2020; 1151707 (2020) https://doi.org/10.1117/12.2574759.

References

1. M.-C. van Lare, F. J. Timmermans, and J. Finders, "Alternative reticles for low-k1 EUV imaging," *Proc. SPIE* **11147**, 111470D (2019).
2. R. Ahrenkiel, "Modified Kramers–Kronig analysis of optical spectra," *J. Opt. Soc. Am.* **61**(12), 1651–1655 (1971).
3. B. L. Henke, E. M. Gullikson, and J. C. Davis, "X-ray interactions: photoabsorption, scattering, transmission, and reflection at e= 50-30,000 ev, z= 1-92," *At. Data Nucl. Data Tables* **54**(2), 181–342 (1993).
4. C.-C. Wu et al., "Lifetime test on EUV photomask with EBL2," *Proc. SPIE* **11178**, 111780E (2019).
5. S. Singh et al., "A study on EUV reticle surface molecular contamination under different storage conditions in a HVM foundry fab," *Proc. SPIE* **10143**, 101431T (2017).
6. R. Jonckheere et al., "Study of EUV reticle storage effects through exposure on EBL2 and NXE," *Proc. SPIE* **11517**, 115170Z (2020).
7. E. M. Gullikson, S. Mrowka, and B. B. Kaufmann, "Recent developments in EUV reflectometry at the advanced light source," *Proc. SPIE* **4343**, 363–373 (2001).
8. A. Aquila et al., "Developments in realistic design for aperiodic Mo/Si multilayer mirrors," *Opt. Express* **14**(21), 10073–10078 (2006).
9. S. Sherwin et al., "Measuring the phase of EUV photomasks," *Proc. SPIE* **11147**, 111471F (2019).
10. D. Attwood and A. Sakdinawat, *X-Rays and Extreme Ultraviolet Radiation: Principles and Applications*, Cambridge University Press (2017).
11. P. B. Mirkarimi, S. Bajt, and M. A. Wall, "Mo/Si and Mo/Be multilayer thin films on Zerodur substrates for extreme-ultraviolet lithography," *Appl. Opt.* **39**(10), 1617–1625 (2000).

12. A. Gibaud and G. Vignaud, "Specular reflectivity from smooth and rough surfaces," in *X-Ray and Neutron Reflectivity*, J. Daillant and A. Gibaud, Eds., pp. 85–131, Springer (2009).
13. C. C. Katsidis and D. I. Siapkas, "General transfer-matrix method for optical multilayer systems with coherent, partially coherent, and incoherent interference," *Appl. Opt.* **41**(19), 3978–3987 (2002).
14. S. Sherwin et al., "Quantitative phase retrieval for EUV photomasks," *Proc. SPIE* **11323**, 1132315 (2020).
15. P. Tseng, "Convergence of a block coordinate descent method for nondifferentiable minimization," *J. Optim. Theory Appl.* **109**(3), 475–494 (2001).
16. W. H. Press et al., *Numerical Recipes 3rd Edition: The Art of Scientific Computing*, Cambridge University Press (2007).
17. Y.-C. Chang, "N-dimension golden section search: its variants and limitations," in *2nd Int. Conf. Biomed. Eng. Inf.*, IEEE, pp. 1–6 (2009).
18. J. Kiefer, "Sequential minimax search for a maximum," *Proc. Am. Math. Soc.* **4**(3), 502–506 (1953).
19. S. Boyd, S. P. Boyd, and L. Vandenberghe, *Convex Optimization*, Cambridge University Press (2004).

Stuart Sherwin received his bachelor's degree in physics and applied mathematics from UC Berkeley in 2013. Following an interlude at KLA in the Reflective Electron Beam Lithography and 5D-Process Control teams, in 2016, he returned to UC Berkeley once again to pursue a PhD in electrical engineering and computer science. Under the direction of Laura Waller, Andy Neureuther, and Patrick Naulleau, his research focuses on applying computational imaging to EUV lithography and metrology.

Markus Benk is the lead scientist of the CXRO EUV mask research and development beamline at the Advanced Light Source, Lawrence Berkeley National Laboratory. He received his diploma in photo engineering from the Cologne University of Applied Sciences in 2006 and his PhD from RWTH Aachen University in 2011. His research interests include sources, metrology and optics for soft x-rays, and extreme ultraviolet light.

Laura Waller is an associate professor of electrical engineering (EE) and computer sciences at UC Berkeley. She received BS, Meng, and PhD degrees from the Massachusetts Institute of Technology and she was a postdoc/lecturer of physics at Princeton University. She is a Packard Fellow, Moore Foundation Data-driven Investigator, Bakar Fellow, OSA Fellow, AIMBE Fellow, and Chan-Zuckerberg Investigator. She recieved the Carol D.Soc Distinguished Graduate Mentoring Award, OSA Adolph Lomb Medal, NSF CAREER Award, and SPIE Early Career Achievement Award.

Andrew Neureuther received his BS, MS, and PhD degrees in EE from the University of Illinois, and joined the faculty in EECS at U.C. Berkeley. His work is mainly in the field of optical, and electron-beam lithography with emphasis on resist modeling, imaging with partial coherence, scattering from topography, TCAD algorithms, and DFM. He received the IEEE Cledo Brunetti Award, the SPIE Zernike Award, and is a member of NAE.

Patrick Naulleau received his BS and MS degrees in electrical engineering from Rochester Institute of Technology, Rochester, New York, and his PhD in electrical engineering from University of Michigan, Ann Arbor. Following graduate school, he joined Berkeley Lab on the EUV LLC program building the world's first EUV scanner. In April 2010, he became director of the Center for X-ray Optics at Berkeley Lab. He has over 350 publications and 19 patents and is a Fellow of OSA and SPIE.